



## Curvilinear manipulation of polarized spin waves

Hongbin Wu (武宏斌) and Jin Lan (兰金) \*

Center for Joint Quantum Studies and Department of Physics, School of Science, Tianjin University,  
92 Weijin Road, Tianjin 300072, China

 (Received 13 December 2021; revised 28 February 2022; accepted 11 May 2022; published 24 May 2022)

Polarization, the precession direction with respect to the background magnetization, is an intrinsic degree of freedom of spin wave. Introducing symmetry-breaking mechanisms lies in the heart of lifting the degeneracy between polarized spin-wave modes and is essential in constructing polarization-based magnonic devices. Here we show that polarized spin waves can be naturally harnessed in a curved antiferromagnetic wire via tuning its curvature and torsion. Specifically, we investigate evolution of polarized spin wave in a spin-wave rotator and a spin-wave interferometer based on magnetic circular helices and correlate these curvilinear effects to the Berry phase accumulated along the wire.

DOI: [10.1103/PhysRevB.105.174427](https://doi.org/10.1103/PhysRevB.105.174427)

### I. INTRODUCTION

Spin wave, the collective precession of ordered magnetizations, is one of the basic excitations in magnetic systems. As an alternative angular momentum carrier beside spin-polarized electron [1,2], spin wave is of crucial importance for both fundamental physics and industrial applications. And since the propagation of the spin wave does not involve physical motion of underlying electrons, magnonics as a field devoted to spin-wave manipulation has attracted remarkable interests in recent years [3–9].

Polarization, denoting the oscillation direction, is an intrinsic property for all waves, including electromagnetic, acoustic as well as spin waves [10–12]. Theoretically, polarization has emerged as a key ingredient in spin-wave field-effect transistor [11], spin-wave polarizer and retarder [12], spin-wave double refraction [13], magnonic spin Nernst effect [14,15], as well as using the spin wave to drive magnetic texture motion [16–20]. In the meantime, recent rapid technical improvements enable the detection of the polarized spin wave in various experiments, including antiferromagnetic spin pumping [21–23], inelastic neutron scattering [24,25], antiferromagnetic resonance [26], and spin signal transmission [27].

Multiple approaches have been proposed to harness the polarized spin wave, e.g., applying an external magnetic field [10], introducing the Dzyaloshinskii-Moriya interaction (DMI) [11], depositing magnetic textures [12,13,19], and streaming electrical current [28]. However, the applicability and efficiencies of these approaches are frequently limited by the magnetic properties and configurations available in realistic materials. A convenient scheme to lift the restrictions is to use curvilinearity embedded in bent wires or curved surfaces, which are ready to prepare in state of art experiments [29–34]. Despite this unique yet powerful scheme in modifying the magnetic properties [35–39], possibilities of using curvilinear

ear effects to harness the polarized spin wave are not fully explored.

In this paper, we investigate the dynamics of polarized spin wave along a curved antiferromagnetic wire, using the language of curvature and torsion. We show that for a magnetic circular helix shifts the phase between left/right circular spin-wave modes due to the emergent Dzyaloshinskii-Moriya interaction. We further propose that a spin-wave rotation based on a single circular helix, and a spin-wave interferometer based two oppositely wound circular helices. Using curvilinear effects for polarization manipulation offers a new paradigm in constructing magnonic logic devices.

The rest of paper is organized as follows. The magnetic dynamics in curved wire is formulated by establishing the connections between curvilinear effect to an emergent Dzyaloshinskii-Moriya interaction in Sec. II. The phase shift of the spin wave experienced in circular helices, the functionalities of the spin-wave rotator and the spin-wave interferometer are studied in Sec. III. Discussions about the connection between torsion and Berry phase as well as a short conclusion are given in Sec. IV.

### II. BASIC MODEL

#### A. Magnetic dynamics in a curved antiferromagnetic wire

Consider a curved antiferromagnetic wire embedded in three-dimensional (3D) space as shown in Fig. 1(a), which is described by the parameterized position  $\mathbf{r}(s)$  with the parameter  $s$  being the arc length of the wire. To describe the dynamics in a curved wire, it is convenient to introduce local curvilinear bases in the Frenet-Serret frame [36,37],

$$\hat{\mathbf{e}}_1 = \mathbf{r}', \quad \hat{\mathbf{e}}_2 = \frac{\hat{\mathbf{e}}_1'}{|\hat{\mathbf{e}}_1'|}, \quad \hat{\mathbf{e}}_3 = \hat{\mathbf{e}}_1 \times \hat{\mathbf{e}}_2, \quad (1)$$

where  $\mathbf{r}' \equiv d\mathbf{r}/ds$  denotes the derivative with respect to the arc length  $s$ ,  $\hat{\mathbf{e}}_{1/2/3}$  are the tangent, normal and binormal vectors of the curve  $\mathbf{r}(s)$  respectively.

\*Corresponding author: lanjin@tju.edu.cn

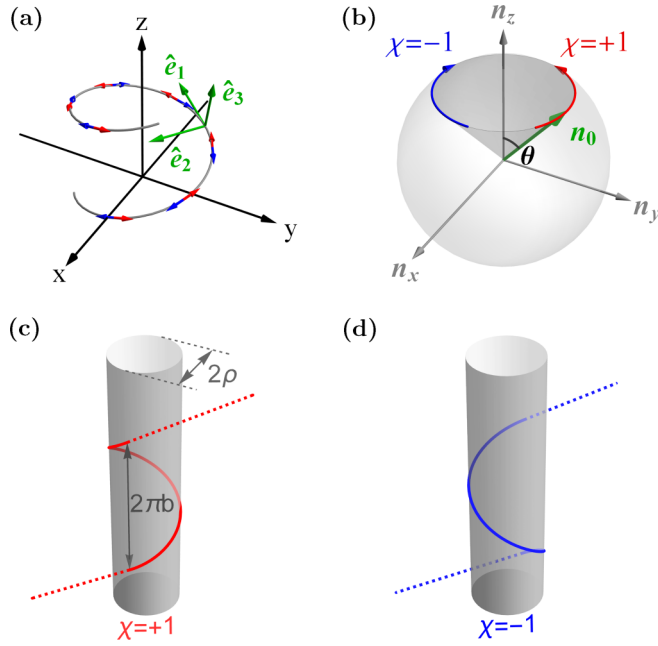


FIG. 1. Schematics of curved magnetic wires. (a) Magnetizations in a curved magnetic wire. The gray line is the curved magnetic wire, the red/blue arrows are the magnetizations in two sublattices, and the three green arrows are the curvilinear bases. (b) Magnetizations in a magnetic Bloch sphere. The anticlockwise/clockwise winding with helicity  $\chi = \pm 1$  are shown in red/blue color. (c) and (d) Space curves of left/right wound circular helices. Dashed lines are straight wires in smooth connection with the circular helix.

We denote the magnetization directions of two sublattices in the curved antiferromagnetic wire by unit vectors  $\mathbf{m}_{1/2}$  as depicted by red/blue arrows in Fig. 1(a). The magnetizations are alternatively described by the staggered Néel order magnetization  $\mathbf{n} = (\mathbf{m}_1 - \mathbf{m}_2)/(|\mathbf{m}_1 - \mathbf{m}_2|)$  and the net magnetization as  $\mathbf{m} = \mathbf{m}_1 + \mathbf{m}_2$ . Under the orthogonal constraint  $\mathbf{n} \cdot \mathbf{m} = 0$ , the dynamics of the staggered order  $\mathbf{n}$  is then governed by [18,40–44]

$$\ddot{\mathbf{n}} \times \mathbf{n} = -\gamma J \mathbf{n} \times (\gamma \mathbf{h} - \alpha \dot{\mathbf{n}}), \quad (2)$$

and  $\mathbf{m} = (\dot{\mathbf{n}} \times \mathbf{n})/\gamma J$  is a slave quantity, where  $\ddot{\mathbf{n}} \equiv \partial_t^2 \mathbf{n}$ ,  $\dot{\mathbf{n}} \equiv \partial_t \mathbf{n}$ ,  $\gamma$  is the gyromagnetic constant, and  $\alpha$  is the Gilbert damping constant. Here  $\mathbf{h} = -(1/\mu_0 M_s \mathcal{A}) \delta U / \delta \mathbf{n}$  is the effective field acting on staggered magnetization  $\mathbf{n}$ , where  $\mu_0$  is the vacuum permeability,  $M_s$  is the saturation magnetization, and  $\mathcal{A}$  is the cross-sectional area of the magnetic wire. The magnetic energy of interest in this paper is  $U = \mathcal{A} \int u ds$  with the energy line density  $u$  described by

$$u(\mathbf{n}, \mathbf{m}) = u_A + u_K + u_m \\ = \frac{\mu_0 M_s}{2} \left[ A (\nabla \mathbf{n})^2 - K (\mathbf{n} \cdot \hat{\mathbf{e}}_1)^2 + \frac{J}{2} |\mathbf{m}|^2 \right], \quad (3)$$

where  $A$  and  $J$  are the inter/intra-sublattice exchange-coupling constants,  $K > 0$  is the (single-ion type [45]) easy-axis anisotropy along the tangential direction  $\hat{\mathbf{e}}_1$  of the wire. In this paper, the long-range dipolar interaction is neglected due to the interweaving sublattices with almost opposite magnetizations in the antiferromagnetic environment.

## B. Emergent Dzyaloshinskii-Moriya interaction and anisotropy

Continuous variations of the curvilinear bases  $\hat{\mathbf{e}}_{1/2/3}$  in Eq. (1) render the physical properties of a curved wire distinct from a straight wire. The differential properties of a curved wire is characterized by the Frenet-Serret formula  $\hat{\mathbf{e}}'_1 = \kappa \hat{\mathbf{e}}_2$ ,  $\hat{\mathbf{e}}'_2 = -\kappa \hat{\mathbf{e}}_1 + \tau \hat{\mathbf{e}}_3$ , and  $\hat{\mathbf{e}}'_3 = -\tau \hat{\mathbf{e}}_2$ , where  $\kappa$  and  $\tau$  are the curvature and torsion of the curved wire [46], respectively. The curvature  $\kappa$  measures the bending of the wire within a plane, while the torsion  $\tau$  measures the twist of the wire out of a specific plane. In vector form, the Frenet-Serret formula reads

$$\hat{\mathbf{e}}'_\beta = \mathbf{d} \times \hat{\mathbf{e}}_\beta, \quad (4)$$

where  $\mathbf{d} = (\tau \hat{\mathbf{e}}_1 + \kappa \hat{\mathbf{e}}_3)$  is the curvilinear vector induced by the spatial variation of the curvilinear basis  $\{\hat{\mathbf{e}}_\beta\}$ ,  $\beta = 1-3$ . The chiral nature of Eq. (4) implies that the magnetic system in a curved wire resides in a local rotating frame with respect to vector  $\mathbf{d}$  [47].

Invoking the Frenet-Serret formula in Eq. (4), the derivative of the staggered magnetization  $\mathbf{n} = \sum_\beta n_\beta \hat{\mathbf{e}}_\beta$  then takes the following co-derivative form

$$\mathbf{n}' \equiv \frac{d\mathbf{n}}{ds} = (\partial_s + \mathbf{d} \times) \mathbf{n}, \quad (5)$$

where  $\partial_s \mathbf{n} \equiv \sum_\beta (\partial_s n_\beta) \hat{\mathbf{e}}_\beta$  denotes the partial derivative solely acting on the magnetization component  $n_\beta$ . Including the co-derivative in Eq. (5), the exchange coupling energy  $u_A$  in Eq. (3) then divides into the following three parts [48],

$$u_A = \tilde{u}_A + \tilde{u}_D + \tilde{u}_K \\ = \frac{\mu_0 M_s}{2} [A (\partial_s \mathbf{n})^2 + 2A \mathbf{d} \cdot (\mathbf{n} \times \partial_s \mathbf{n}) - A (\mathbf{d} \cdot \mathbf{n})^2], \quad (6)$$

where an effective DMI in vector  $\mathbf{D} = 2A \mathbf{d}$  as well as an effective easy-axis anisotropy of strength  $A$  with respect to vector  $\mathbf{d}$ , arise besides the normal exchange coupling in terms of  $\partial_s \mathbf{n}$  [33,36,37]. The above DMI energy is of homogeneous type, and is different from the DMI energy of inhomogeneous type [17,49] in the form  $\tilde{\mathbf{D}} \cdot (\mathbf{n} \times \mathbf{m})$ , which is the origin of the weak ferromagnetism in antiferromagnets.

In Eq. (6), the DM vector is explicitly written as

$$\mathbf{D} = 2A\tau \hat{\mathbf{e}}_1 + 2A\kappa \hat{\mathbf{e}}_3, \quad (7)$$

indicating that the torsion  $\tau$  and curvature  $\kappa$  determine the DM strength with respect to the tangential/binormal directions  $\hat{\mathbf{e}}_{1/3}$ , respectively. The strength of emergent DMI in Eq. (6) is proportional to the exchange-coupling constant  $A$ , similar to the DMI caused by the spin-orbit coupling in heavy-metal materials or the heterostructure interface [50]. In addition, the DMI caused by curvilinear effects here also shares much similarity with the geodesic effects due to geometric space-time distortion in general relativity [51]. In this sense, modifying the effective space-time metric for magnetic dynamics via strain or magnon-phonon interaction is expected to alter this emergent DMI [49,52].

On the other hand, from Eqs. (3) and (4), the overall energy density of magnetic anisotropy is described by

$$u_K + \tilde{u}_K = -\frac{\mu_0 M_s}{2} [K n_1^2 + A(\tau n_1 + \kappa n_3)^2], \quad (8)$$

where the torsion  $\tau$  leads to an enhanced easy-axis anisotropy  $K \rightarrow K + A\tau^2$ , whereas the curvature  $\kappa$  causes a small tilting of the magnetic easy axis toward the binomial direction  $\hat{\mathbf{e}}_3$ .

In experimental practice, the wire is supposed to bend only slowly in comparison the characteristic length of the magnetic system:  $\kappa, \tau \ll 1/W$  with  $W \equiv \sqrt{A/K}$ , hence, the relation  $A\kappa^2 \ll K$  gives rise to negligible tilting of the magnetic easy axis. In the meantime, the anisotropy also dominates the emergent DMI, therefore, homogeneous magnetizations along the magnetic easy-axis  $\mathbf{n}_0 = \hat{\mathbf{e}}_1$  maintain to be the ground state in the curved wire. Inhomogeneous magnetic textures, such as the domain wall may also arise upon curved magnetic wire, but are beyond the scope of this paper and thus omitted. It is noteworthy that the physical settings here are distinct from Ref. [48] where the intrinsic anisotropy is negligible  $K \approx 0$ , and bending is remarkable  $\kappa, \tau \approx 1/W$ . As a result, the magnetization strongly tilts, and even the ground magnetization configuration may turn from homogenous to periodic.

### C. Dynamics of the spin wave in a curved antiferromagnetic wire

When time evolution is involved, the total staggered magnetization  $\mathbf{n}(t)$  naturally separates into the static background  $\mathbf{n}_0$  and the fast precessing spin wave  $\delta\mathbf{n}$ :  $\mathbf{n} = \mathbf{n}_0 + \delta\mathbf{n}$ . Due to unity constraint  $|\mathbf{n}| = 1$ , the spin wave is orthogonal to the background magnetization with  $\mathbf{n}_0 \cdot \delta\mathbf{n} = 0$  satisfied everywhere. Upon the homogenous magnetization  $\mathbf{n}_0 = \hat{\mathbf{e}}_1$  along the tangential direction, the spin wave is written as  $\delta\mathbf{n} = n_2\hat{\mathbf{e}}_2 + n_3\hat{\mathbf{e}}_3$ , i.e., the spin wave oscillates in the normal and binormal directions of the wire. In an equivalent form, the spin wave is denoted by the complex field  $\psi_\sigma = n_2 - i\sigma n_3$  with the chirality  $\sigma = \mp 1$  the left/right circularly polarized spin waves, respectively. Adopting the small amplitude limit  $|n_{2/3}| \ll 1$ , the spin-wave dynamics in the curved wire is recast from Eq. (2) to

$$-\ddot{\psi}_\sigma = \gamma^2 J [A(i\partial_s + \sigma\tau)^2 + K] \psi_\sigma + \alpha\gamma J \dot{\psi}_\sigma, \quad (9)$$

where the degeneracy of two circular polarizations are lifted by the torsion  $\tau$ . The curvature  $\kappa$  does not participate into Eq. (9) since the DMI orthogonal to the static magnetization direction does not affect the spin-wave dynamics in the linear regime [53].

The spin-wave dispersion corresponding to Eq. (9) is

$$\omega_\sigma = \gamma \sqrt{J[A(k_\sigma - \sigma\tau)^2 + K] - \frac{\alpha^2 J^2}{4} - \frac{i\alpha\gamma J}{2}}, \quad (10)$$

where  $\omega_\sigma$  and  $k_\sigma$  with  $\sigma = \mp 1$  are the spin-wave frequency and wave vector for left/right circular modes, respectively. In comparison, for a straight wire with vanishing torsion  $\tau = 0$ , the dispersion reduces to  $\omega_0 = \gamma \sqrt{J(Ak_0^2 + K) - (\alpha^2 J^2)/4} - i\alpha\gamma J/2$ . Therefore, in reference to the straight wire with fixed spin-wave frequency  $\omega$ , the wave vector of the spin wave in a curved wire is shifted by [11]

$$\Delta k \equiv k_\sigma - k_0 = \sigma\tau, \quad (11)$$

i.e., the wave vector of the left/right circular modes with  $\sigma = \mp 1$  are shifted in opposite directions by the same amount of  $|\tau|$ . It is noteworthy that the wave-vector shift  $\Delta k$  is

independent of the spin-wave frequency  $\omega$  and the detailed magnetic parameters  $A$ ,  $K$ , and  $J$  in Eq. (3).

## III. POLARIZED SPIN WAVE ALONG CIRCULAR HELICES

### A. Basic properties of a circular helix

The simplest wire with finite curvature and torsion is a circular helix [54], which is virtually wound upon a cylinder as schematically shown in Figs. 1(c) and 1(d). The 3D space curve of a circular helix is parametrized by

$$\mathbf{r}(s) = \left[ \rho \cos\left(\frac{s}{r}\right), \chi \rho \sin\left(\frac{s}{r}\right), \frac{bs}{r} \right], \quad (12)$$

where  $\rho$  is the radius,  $b$  is the reduced pitch,  $r = \sqrt{\rho^2 + b^2}$  is the parametric radius, and  $\chi = \mp 1$  is the helicity for left/right-handed helices. The tangent vector of a circular helix is described by  $\hat{\mathbf{e}}_1 = [-\rho \sin(s/r), \chi \rho \cos(s/r), b]/r$ , which has a periodicity of  $2\pi r$ , and all tangent vectors form a constant polar angle  $\theta = \arccos(\hat{\mathbf{e}}_1 \cdot \hat{\mathbf{z}}) = \arccos(b/r)$  with respect to the  $\hat{\mathbf{z}}$  direction. Therefore, a collection of magnetizations lying in tangent vectors of circular helix forms a cone in a magnetic Bloch sphere with apex semiangle  $\theta$  as shown in Fig. 1(b).

From Eq. (12), the curvature and torsion of a helix are constants with

$$\kappa = \frac{\rho}{r^2}, \quad \tau = \frac{\chi b}{r^2}, \quad (13)$$

where the curvature  $\kappa$  is controlled by the radius  $\rho$ , whereas the torsion  $\tau$  is related to the reduced pitch  $b$  as well as the helicity  $\chi$ . The curvature and torsion are intimately connected with the polar angle  $\theta$  via the relation  $\kappa r = \sin\theta$  and  $\tau r = \chi \cos\theta$ , hence the curvature  $\kappa$  (torsion  $\tau$ ) increases/decreases as the polar angle  $\theta$  increases.

According to Eqs. (11) and (13), when a circular spin wave with chirality  $\sigma = \pm 1$  travels along the circular helix with helicity  $\chi = \pm 1$ , the phase shift accumulated in one coil of length  $2\pi r$  is then

$$\Delta\phi = \int_0^{2\pi r} \Delta k ds = 2\pi r \sigma \tau = 2\pi \sigma \chi \cos\theta, \quad (14)$$

which is simultaneously controlled by both spin-wave chirality  $\sigma$  and the winding helicity  $\chi$ . By flipping either the spin-wave chirality  $\sigma$  or the winding helicity  $\chi$ , the phase-shift  $\Delta\phi$  is flipped; or alternatively speaking, the phase difference between the two opposite chirality or the helicity is  $2|\Delta\phi| = 4\pi \cos\theta$ . With this additional phase  $\Delta\phi$ , we proceed to investigate the evolution of polarized spin wave advancing along magnetic circular helices.

### B. Spin-wave rotator with a single circular helix

Consider a linearly polarized spin wave, which consists of equal components of both circular polarizations, propagates along a magnetic circular helix. According to Eq. (14), the left/right circular components experience opposite phase shifts  $\pm|\Delta\phi|$ , leading to a rotation of the polarization direction for the linear spin wave [7,11,28,55], i.e., spin-wave Faraday effect arises in a magnetic circular helix. The rotation angle

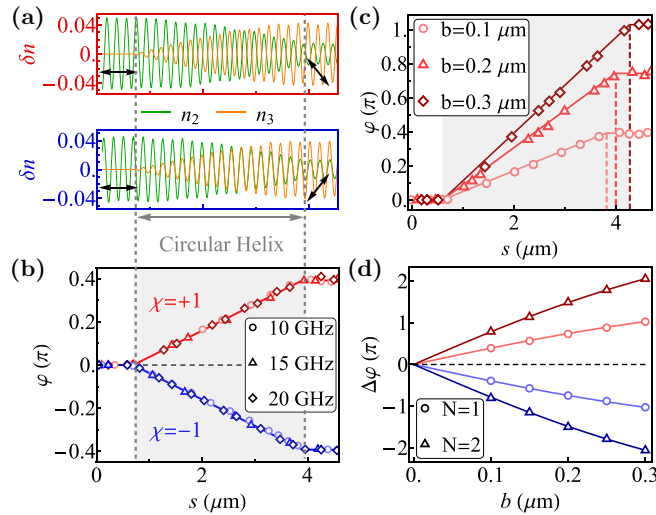


FIG. 2. Micromagnetic simulations of spin-wave rotation based on a magnetic circular helix. (a) Spatial profiles of spin wave across a magnetic helix with  $\chi = \pm 1$  in upper/lower panels. Two spin-wave components  $n_{2/3}$  are plotted in green/orange lines, and the arrows denote the polarization direction in two sides. (b) Spatial evolutions of polarization angle  $\varphi$  as a function of arc length  $s$  for three different frequencies  $f = 10, 15,$  and  $20$  GHz. (c) Spatial profiles of polarization angle  $\varphi$  for different reduced pitch  $b$ . (d) The overall rotation angle  $\Delta\varphi$  as a function of reduced pitch  $b$  for 1 (2) coils of magnetic helices. For (b)–(d), the dots are extracted from micromagnetic simulations, the lines are theoretical calculations based on Eq. (15), and the red/blue lines are for magnetic helix with helicity  $\chi = \pm 1$ . The default size of the circular helix is with the radius  $\rho = 0.5 \mu\text{m}$  and the reduced pitch  $b = 0.1 \mu\text{m}$ .

of the linear spin wave, which takes half of the phase difference between its left and right circular components, is then described by

$$\Delta\varphi = 2\pi\chi \cos\theta, \quad (15)$$

where the rotation angle  $\Delta\varphi$  flips its sign for oppositely wound helices with  $\chi = \pm 1$ . The rotation angle is directly proportional to the polar angle  $\theta$  of the helix, highlighting the critical role of torsion (or the emergent DMI) in spin-wave rotation.

The evolutions of a linearly polarized spin wave across a circular helix between two straight wires as extracted from micromagnetic simulations, are plotted in Fig. 2(a). As a linear spin wave with purely  $n_2$  component passes across the right/left wound helix with helicity  $\chi = \pm 1$ , the spin wave gradually acquires an out-of-phase (in-phase)  $n_3$  component. Consequently, in Fig. 2(b), the polarization angles  $\varphi$  increases/decreases steadily within the right/left wound circular helix of helicity  $\chi = \pm 1$ , and level off in straight wires. The linear spin wave finally acquires an anticlockwise/clockwise rotation angle of about  $0.4\pi$ , in good agreement with the theoretical value of  $\Delta\varphi = 0.392\pi$  calculated from Eq. (15). In addition, the spatial profiles for three different spin-wave frequencies  $f = 10, 15,$  and  $20$  GHz overlap with each other, confirming the frequency-independent feature of spin-wave rotation in a circular helix. By increasing the reduced pitch  $b$  from  $0.1$  to  $0.2 \mu\text{m}$  ( $0.3 \mu\text{m}$ ), the rotation angle also roughly

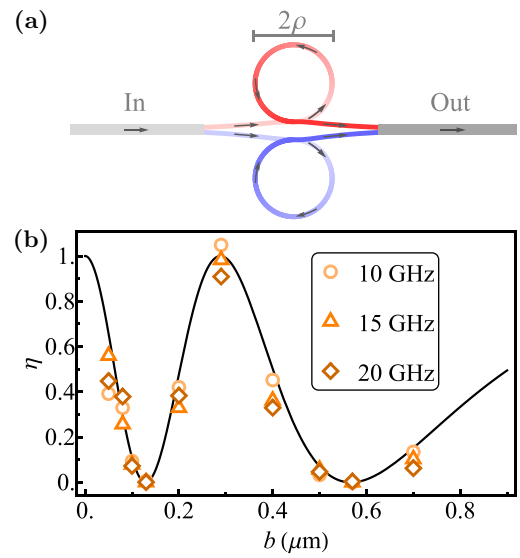


FIG. 3. Micromagnetic simulations of the spin-wave interference upon two oppositely wound helices. (a) Schematics of a spin-wave interferometer based on circular helices. The gray blocks are the input/output ports, the red/blue curves denote two arms upon circular helices of helicity  $\chi = \pm 1$ , the darkness encodes the height information, and the arrows mark the flow directions. (b) The output efficiency  $\eta$  as a function of reduced pitch  $b$ . The dots are extracted from micromagnetic simulations, and the solid line is theoretically calculated from Eq. (16). In (b), an intensity reduction by a ratio of about  $0.34$ , caused by signal reflections in imperfect junctions, is preexcluded in the estimation of the output efficiency.

multiplies by about  $1.9$  ( $2.6$ ) times in Fig. 2(c); and the rotation angles double for a circular helix of  $N = 2$  coils as shown in Fig. 2(d). All above behaviors highlight the critical role of the torsion in rotating the polarization direction of a linear spin wave.

### C. Spin-wave interferometer with two oppositely wound circular helices

Consider a Mach-Zehnder type spin-wave interferometer in Fig. 3(a), which uses a left/right-handed magnetic helices as its two arms. Due to symmetry of its two arms, the polarized spin wave is split equally into two arms, and merged again in the output port. According to Eq. (14), the phase shifts of circular spin waves in these two arms are opposite, leading to an overall phase difference of  $2|\Delta\phi|$ . Consequently, the interference of spin waves in two arms leads to

$$\eta = \cos^2(\Delta\phi) = \cos^2(2\pi \cos\theta), \quad (16)$$

where  $\eta$  is the output efficiency measuring the ratio of the output intensity relative to the input intensity. Despite that Eq. (16) is originally derived for circular spin waves, it naturally extends to arbitrarily polarized spin wave, for which the intensity is simply the summation of its two circular components [56].

The output efficiency  $\eta$  extracted from micromagnetic simulations as a function of reduced pitch  $b$  for a fixed helix radius  $\rho = 0.5 \mu\text{m}$  are overlaid well with theoretical lines explicitly given by  $\eta = \cos^2(2\pi b/\sqrt{\rho^2 + b^2})$  from Eq. (16). Whereas

the modulation becomes slightly inefficient as  $b$  increases due to the accompanying increment of parametric radius  $r$ , two complete destruction points with  $\eta = 0$  are established at  $b \approx 0.13$  and  $b \approx 0.57 \mu\text{m}$ . Similar to the spin-wave rotation in Fig. 2(b), the intensity modulation is the same for three spin-wave frequencies  $f = 10, 15,$  and  $20$  GHz, and we have additionally checked that the intensity modulations are roughly the same for circularly, linearly, and elliptically polarized spin waves.

#### IV. DISCUSSION AND CONCLUSION

The phase difference  $\Delta\phi$  in Eq. (14), which is solely connected to the polar angle  $\theta$  but irrelevant to detailed magnetic parameters, is intimately correlated to the Berry phase acquired along the helix [57–59]. The circular spin wave  $|\psi(\mathbf{n}_0, \sigma)\rangle$  has its chiral operator  $\hat{\sigma}$  always parallel to the background magnetization  $\mathbf{n}_0$ , which is governed by

$$\mathbf{n}_0 \cdot \hat{\sigma} |\psi[\mathbf{n}_0(s), \sigma]\rangle = \sigma |\psi[\mathbf{n}_0(s), \sigma]\rangle, \quad (17)$$

where the chiral operator  $\hat{\sigma}$  is modulated by an effective magnetic field in  $\mathbf{n}_0$ . After traveling along one coil of the circular helix, the staggered magnetization  $\mathbf{n}_0$  restores its original direction, whereas the spin wave  $|\psi(\mathbf{n}_0(s), \sigma)\rangle$  acquires an additional phase factor  $\exp(-i\sigma\Omega)$ , where  $\Omega$  is the solid angle subtended by the static magnetization  $\mathbf{n}_0$  in the Bloch sphere [57,60]. The total solid angle for the cone in Fig. 1(b) is  $\Omega = 2\pi\chi(1 - \cos\theta)$ , which differs from Eq. (14) only by a trivial value of  $2\pi$ . In this sense, the torsion  $\tau$  in the curvilinear wire acts as a local Berry curvature as spin wave propagates along a curved wire.

In conclusion, we demonstrate that the curvilinear effects of magnetic wires provide extrinsic yet universal means to manipulate the polarized spin wave. Specifically, the spin-wave rotator and interferometer upon magnetic helices are proposed due to the additional phase caused by the interplay between the wire winding helicity and the spin-wave chirality. Based on close relations between curvilinearity and magnetism, controlling magnetic functionalities via mechanical means is also envisioned.

#### ACKNOWLEDGMENT

This work was supported by National Natural Science Foundation of China (Grant No. 11904260) and Natural Science Foundation of Tianjin (Grant No. 20JCQNJC02020).

#### APPENDIX A: MICROMAGNETIC SIMULATIONS

The micromagnetic simulations are based on a synthetic antiferromagnetic wire, which consists of two coupled antiferromagnetically ferromagnetic yttrium iron garnet  $\text{Y}_3\text{Fe}_5\text{O}_{12}$  wires [12,18,61]. The dynamics of the synthetic antiferromagnet wire is governed by two coupled Landau-Lifshitz-Gilbert (LLG) equations,

$$\dot{\mathbf{m}}_i = -\gamma \mathbf{m}_i \times \mathbf{h}_i + \alpha \mathbf{m}_i \times \dot{\mathbf{m}}_i, \quad (\text{A1})$$

where  $i = 1, 2$  denotes two sublattices residing in two ferromagnetic wires, respectively. Here  $\mathbf{h}_i = A\nabla^2 \mathbf{m}_i + K(\mathbf{m}_i \cdot \hat{\mathbf{e}}_1)\hat{\mathbf{e}}_1 + 2J\mathbf{m}_i$  (with  $\bar{1} = 2, \bar{2} = 1$ ) is the effective magnetic

field on sublattice magnetization  $\mathbf{m}_i$ , where  $A$  is the exchange-coupling constant within each sublattice,  $K$  is the easy-axis anisotropy along the tangential direction  $\hat{\mathbf{e}}_1$ , and  $J$  is the exchange-coupling constant between two sublattices.

The micromagnetic simulations are performed in COMSOL MULTIPHYSICS [62] where the LLG equation (A1) is transformed to a weak form. The simulations in Fig. 2 are based on the structures in Figs. 1(c) and 1(d), the simulations in Fig. 3(b) are based on the structure shown in Fig. 3(a), and all structures are directly constructed using the embedded parametric functions in COMSOL MULTIPHYSICS. The magnetic parameters adopted in the simulations are as follows: the intralayer exchange-coupling constant  $A = 3.28 \times 10^{-11}$  A m, the interlayer coupling constant  $J = 5 \times 10^5$  A/m, the anisotropy  $K = 3.88 \times 10^4$  A/m, and the damping constant  $\alpha = 1 \times 10^{-4}$ .

In Fig. 2, the spin wave  $\delta\mathbf{n}$  in simulations is obtained by subtracting the current magnetization  $\mathbf{n}$  by the static magnetization  $\mathbf{n}_0$  at  $t = 0$ :  $\delta\mathbf{n} = \mathbf{n} - \mathbf{n}_0$ . Then using the local curvilinear directions  $\hat{\mathbf{e}}_{1/2/3}$  calculated from the parametric functions, the spin-wave components  $n_{2/3} \equiv \delta\mathbf{n} \cdot \hat{\mathbf{e}}_{2/3}$  are extracted. The polarization angle  $\varphi$  is obtained using the relation  $\varphi = \arccos(n_2/\sqrt{n_2^2 + n_3^2})$  for the linearly polarized spin wave.

In Fig. 3, the spin wave is continuously excited with a fixed intensity  $I_{\text{in}}$  in the input port, and then the spin-wave intensity  $I_{\text{out}}$  is monitored at the fixed point in the output port, after enough waiting time. The output intensity  $I_{\text{out}}$  is recorded for each simulation with only the reduced pitch  $b$  is varied. The output efficiency  $\eta$  is then calculated using  $\eta = I_{\text{out}}/I_{\text{out}}^{\text{max}}$ , where  $I_{\text{out}}^{\text{max}} \approx 0.34I_{\text{in}}$  is the maximum intensity among all possible values of reduced pitch  $b$ .

#### APPENDIX B: TRANSFORMATION TO DYNAMICS OF STAGGERED MAGNETIZATION

The dynamics of sublattice magnetization in Eq. (A1) can be transformed to the dynamics of staggered magnetization in Eq. (2) with the aid of Lagrangian theory [40–42,44,49].

The Lagrangian corresponding to Eq. (A1) is [44,49]

$$\mathcal{L} = \frac{S}{2\gamma} \int [\mathbf{a}_1(\mathbf{m}_1) \cdot \dot{\mathbf{m}}_1 + \mathbf{a}_2(\mathbf{m}_2) \cdot \dot{\mathbf{m}}_2] ds - U(\mathbf{m}_1, \mathbf{m}_2), \quad (\text{B1})$$

where  $S = \mu_0 M_s \mathcal{A}$  is the magnetic flux,  $\mathbf{a}(\mathbf{m}) = (\boldsymbol{\Omega} \times \mathbf{m}) / (1 + \boldsymbol{\Omega} \times \mathbf{m})$  is the vector potential for a monopole with arbitrary direction  $\boldsymbol{\Omega}$ , and

$$U(\mathbf{m}_1, \mathbf{m}_2) = \frac{S}{4} \sum_{i=1,2} \int [A(\nabla \mathbf{m}_i)^2 - K(\mathbf{m}_i \cdot \hat{\mathbf{e}}_1)^2 + 2J\mathbf{m}_i \cdot \mathbf{m}_i] ds \quad (\text{B2})$$

is the total magnetic energy. Besides, the Rayleigh dissipation function is

$$\mathcal{R} = \frac{\alpha S}{4\gamma} \int [|\dot{\mathbf{m}}_1|^2 + |\dot{\mathbf{m}}_2|^2] ds. \quad (\text{B3})$$

For transformation, we use the relations  $\mathbf{n} = (\mathbf{m}_1 - \mathbf{m}_2)/2$  and  $\mathbf{m} = \mathbf{m}_1 + \mathbf{m}_2$ , and furthermore, we set  $\mathbf{a}_i(\mathbf{m}) = \mathbf{a}(\mathbf{m})$

and  $\mathbf{a}_2 = \mathbf{a}(-\mathbf{m})$ . Then the Lagrangian in Eq. (B1) is transformed to

$$\mathcal{L} = \frac{S}{2\gamma} \int [\dot{\mathbf{n}} \cdot (\mathbf{n} \times \mathbf{m})] ds - U(\mathbf{n}, \mathbf{m}), \quad (\text{B4})$$

where only the first order of  $\mathbf{m}$  is retained for the kinetic term. Furthermore, the magnetic energy is transformed to

$$\begin{aligned} U(\mathbf{n}, \mathbf{m}) &= U(\mathbf{n}) + U(\mathbf{m}) \\ &= \frac{S}{2} \int [A(\nabla \mathbf{n})^2 - K(\mathbf{n} \cdot \hat{\mathbf{e}}_1)^2] ds \\ &\quad + \frac{S}{4} \int J|\mathbf{m}|^2 ds, \end{aligned} \quad (\text{B5})$$

where only the term in  $|\mathbf{m}|^2$  retained for  $U(\mathbf{m})$ , and all cross terms in  $\mathbf{n}$  and  $\mathbf{m}$  are neglected. From Eq. (B4), the dynamics of  $\mathbf{m}$  is then governed by

$$\mathbf{m} = \frac{1}{\gamma J} \dot{\mathbf{n}} \times \mathbf{n}, \quad (\text{B6})$$

and the Lagrangian purely for  $\mathbf{n}$  is recast from Eq. (B4) to

$$\mathcal{L} = \frac{S}{2\gamma^2 J} \int |\dot{\mathbf{n}}|^2 ds - U(\mathbf{n}). \quad (\text{B7})$$

Similarly, the Rayleigh dissipation function is recast from Eq. (B3) to

$$\mathcal{R} = \frac{\alpha S}{2\gamma} \int |\dot{\mathbf{n}}|^2 ds, \quad (\text{B8})$$

where cross terms between  $\mathbf{n}$  and  $\mathbf{m}$  as well terms purely in  $\mathbf{m}$  are again neglected. The Euler-Lagrangian variation of Eqs. (B7) and (B8) with respect to  $\mathbf{n}$  under the constraint  $|\mathbf{n}| = 1$  then yields Eq. (2) in the main text.

- 
- [1] Y. Kajiwara, K. Harii, S. Takahashi, J. Ohe, K. Uchida, M. Mizuguchi, H. Umezawa, H. Kawai, K. Ando, K. Takanashi, S. Maekawa, and E. Saitoh, Transmission of electrical signals by spin-wave interconversion in a magnetic insulator, *Nature (London)* **464**, 262 (2010).
- [2] L. J. Cornelissen, J. Liu, R. A. Duine, J. B. Youssef, and B. J. van Wees, Long-distance transport of magnon spin information in a magnetic insulator at room temperature, *Nat. Phys.* **11**, 1022 (2015).
- [3] V. V. Kruglyak, S. O. Demokritov, and D. Grundler, Magnonics, *J. Phys. D: Appl. Phys.* **43**, 264001 (2010).
- [4] A. V. Chumak, V. I. Vasyuchka, A. A. Serga, and B. Hillebrands, Magnon spintronics, *Nat. Phys.* **11**, 453 (2015).
- [5] J. Lan, W. Yu, R. Wu, and J. Xiao, Spin-Wave Diode, *Phys. Rev. X* **5**, 041049 (2015).
- [6] J. Han, P. Zhang, J. T. Hou, S. A. Siddiqui, and L. Liu, Mutual control of coherent spin waves and magnetic domain walls in a magnonic device, *Science* **366**, 1121 (2019).
- [7] W. Yu, J. Lan, and J. Xiao, Magnetic Logic Gate Based on Polarized Spin Waves, *Phys. Rev. Applied* **13**, 024055 (2020).
- [8] H. Yu, J. Xiao, and H. Schultheiss, Magnetic texture based magnonics, *Phys. Rep.* **905**, 1 (2021).
- [9] A. Barman, G. Gubbiotti, S. Ladak, A. O. Adeyeye, M. Krawczyk, J. Gräfe, C. Adelmann, S. Cotozana, A. Naeemi, V. I. Vasyuchka, B. Hillebrands, S. A. Nikitov, H. Yu, D. Grundler, A. V. Sadovnikov, A. A. Grachev, S. E. Sheshukova, J.-Y. Duquesne, M. Marangolo, G. Csaba *et al.*, The 2021 magnonics roadmap, *J. Phys.: Condens. Matter* **33**, 413001 (2021).
- [10] F. Keffer and C. Kittel, Theory of antiferromagnetic resonance, *Phys. Rev.* **85**, 329 (1952).
- [11] R. Cheng, M. W. Daniels, J.-G. Zhu, and D. Xiao, Antiferromagnetic spin wave field-effect transistor, *Sci. Rep.* **6**, 24223 (2016).
- [12] J. Lan, W. Yu, and J. Xiao, Antiferromagnetic domain wall as spin wave polarizer and retarder, *Nat. Commun.* **8**, 178 (2017).
- [13] J. Lan, W. Yu, and J. Xiao, Geometric magnonics with chiral magnetic domain walls, *Phys. Rev. B* **103**, 214407 (2021).
- [14] R. Cheng, S. Okamoto, and D. Xiao, Spin Nernst Effect of Magnons in Collinear Antiferromagnets, *Phys. Rev. Lett.* **117**, 217202 (2016).
- [15] V. A. Zyuzin and A. A. Kovalev, Magnon Spin Nernst Effect in Antiferromagnets, *Phys. Rev. Lett.* **117**, 217203 (2016).
- [16] E. G. Tveten, A. Qaiumzadeh, and A. Brataas, Antiferromagnetic Domain Wall Motion Induced by Spin Waves, *Phys. Rev. Lett.* **112**, 147204 (2014).
- [17] A. Qaiumzadeh, L. A. Kristiansen, and A. Brataas, Controlling chiral domain walls in antiferromagnets using spin-wave helicity, *Phys. Rev. B* **97**, 020402(R) (2018).
- [18] W. Yu, J. Lan, and J. Xiao, Polarization-selective spin wave driven domain-wall motion in antiferromagnets, *Phys. Rev. B* **98**, 144422 (2018).
- [19] M. W. Daniels, W. Yu, R. Cheng, J. Xiao, and D. Xiao, Topological spin Hall effects and tunable skyrmion Hall effects in uniaxial antiferromagnetic insulators, *Phys. Rev. B* **99**, 224433 (2019).
- [20] S.-H. Oh, S. K. Kim, J. Xiao, and K.-J. Lee, Bidirectional spin-wave-driven domain wall motion in ferrimagnets, *Phys. Rev. B* **100**, 174403 (2019).
- [21] R. Cheng, J. Xiao, Q. Niu, and A. Brataas, Spin Pumping and Spin-Transfer Torques in Antiferromagnets, *Phys. Rev. Lett.* **113**, 057601 (2014).
- [22] P. Vaidya, S. A. Morley, J. van Tol, Y. Liu, R. Cheng, A. Brataas, D. Lederman, and E. del Barco, Subterahertz spin pumping from an insulating antiferromagnet, *Science* **368**, 160 (2020).
- [23] J. Li, C. B. Wilson, R. Cheng, M. Lohmann, M. Kavand, W. Yuan, M. Aldosary, N. Agladze, P. Wei, M. S. Sherwin, and J. Shi, Spin current from sub-terahertz-generated antiferromagnetic magnons, *Nature (London)* **578**, 70 (2020).
- [24] G. Gitgeatpong, Y. Zhao, P. Piyawongwatthana, Y. Qiu, L. W. Harriger, N. P. Butch, T. J. Sato, and K. Matan, Nonreciprocal Magnons and Symmetry-Breaking in the Noncentrosymmetric Antiferromagnet, *Phys. Rev. Lett.* **119**, 047201 (2017).
- [25] Y. Nambu, J. Barker, Y. Okino, T. Kikkawa, Y. Shiomi, M. Enderle, T. Weber, B. Winn, M. Graves-Brook, J. M.

- Tranquada, T. Ziman, M. Fujita, G. E. W. Bauer, E. Saitoh, and K. Kakurai, Observation of Magnon Polarization, *Phys. Rev. Lett.* **125**, 027201 (2020).
- [26] D. MacNeill, J. T. Hou, D. R. Klein, P. Zhang, P. Jarillo-Herrero, and L. Liu, Gigahertz Frequency Antiferromagnetic Resonance and Strong Magnon-Magnon Coupling in the Layered Crystal  $\text{CrCl}_3$ , *Phys. Rev. Lett.* **123**, 047204 (2019).
- [27] J. Han, P. Zhang, Z. Bi, Y. Fan, T. S. Safi, J. Xiang, J. Finley, L. Fu, R. Cheng, and L. Liu, Birefringence-like spin transport via linearly polarized antiferromagnetic magnons, *Nat. Nanotechnol.* **15**, 563 (2020).
- [28] I. Proskurin, R. L. Stamps, A. S. Ovchinnikov, and J.-I. Kishine, Spin-Wave Chirality and Its Manifestations in Antiferromagnets, *Phys. Rev. Lett.* **119**, 177202 (2017).
- [29] F. Balhorn, S. Mansfeld, A. Krohn, J. Topp, W. Hansen, D. Heitmann, and S. Mendach, Spin-Wave Interference in Three-Dimensional Rolled-Up Ferromagnetic Microtubes, *Phys. Rev. Lett.* **104**, 037205 (2010).
- [30] E. J. Smith, D. Makarov, S. Sanchez, V. M. Fomin, and O. G. Schmidt, Magnetic Microhelix Coil Structures, *Phys. Rev. Lett.* **107**, 097204 (2011).
- [31] S. Da Col, S. Jamet, N. Rougemaille, A. Locatelli, T. O. Mentès, B. S. Burgos, R. Afid, M. Darques, L. Cagnon, J. C. Toussaint, and O. Fruchart, Observation of Bloch-point domain walls in cylindrical magnetic nanowires, *Phys. Rev. B* **89**, 180405(R) (2014).
- [32] J.-S. Kim, M.-A. Mawass, A. Bisig, B. Krüger, R. M. Reeve, T. Schulz, F. Büttner, J. Yoon, C.-Y. You, M. Weigand, H. Stoll, G. Schütz, H. J. M. Swagten, B. Koopmans, S. Eisebitt, and M. Kläui, Synchronous precessional motion of multiple domain walls in a ferromagnetic nanowire by perpendicular field pulses, *Nat. Commun.* **5**, 3429 (2014).
- [33] R. Streubel, P. Fischer, F. Kronast, V. P. Kravchuk, D. D. Sheka, Y. Gaididei, O. G. Schmidt, and D. Makarov, Magnetism in curved geometries, *J. Phys. D: Appl. Phys.* **49**, 363001 (2016).
- [34] O. M. Volkov, A. Kákay, F. Kronast, I. Mönch, M.-A. Mawass, J. Fassbender, and D. Makarov, Experimental Observation of Exchange-Driven Chiral Effects in Curvilinear Magnetism, *Phys. Rev. Lett.* **123**, 077201 (2019).
- [35] M. Yan, C. Andreas, A. Kákay, F. García-Sánchez, and R. Hertel, Fast domain wall dynamics in magnetic nanotubes: Suppression of Walker breakdown and Cherenkov-like spin wave emission, *Appl. Phys. Lett.* **99**, 122505 (2011).
- [36] Y. Gaididei, V. P. Kravchuk, and D. D. Sheka, Curvature Effects in Thin Magnetic Shells, *Phys. Rev. Lett.* **112**, 257203 (2014).
- [37] D. D. Sheka, V. P. Kravchuk, and Y. Gaididei, Curvature effects in statics and dynamics of low dimensional magnets, *J. Phys. A: Math. Theor.* **48**, 125202 (2015).
- [38] J. A. Otálora, M. Yan, H. Schultheiss, R. Hertel, and A. Kákay, Curvature-Induced Asymmetric Spin-Wave Dispersion, *Phys. Rev. Lett.* **117**, 227203 (2016).
- [39] D. Makarov, O. M. Volkov, A. Kákay, O. V. Pylypovskiy, B. Budinská, and O. V. Dobrovolskiy, New dimension in magnetism and superconductivity: 3D and curvilinear nanoarchitectures, *Adv. Mater.* **34**, 2101758 (2022).
- [40] A. F. Andreev and V. I. Marchenko, Symmetry and the macroscopic dynamics of magnetic materials, *Sov. Phys.-Usp.* **23**, 21 (1980).
- [41] I. V. Bar'yakhtar and B. A. Ivanov, Nonlinear waves in antiferromagnets, *Solid State Commun.* **34**, 545 (1980).
- [42] F. D. M. Haldane, Nonlinear Field Theory of Large-Spin Heisenberg Antiferromagnets: Semiclassically Quantized Solitons of the One-Dimensional Easy-Axis Néel State, *Phys. Rev. Lett.* **50**, 1153 (1983).
- [43] E. G. Tveten, A. Qaiumzadeh, O. A. Tretiakov, and A. Brataas, Staggered Dynamics in Antiferromagnets by Collective Coordinates, *Phys. Rev. Lett.* **110**, 127208 (2013).
- [44] S. K. Kim, Y. Tserkovnyak, and O. Tchernyshyov, Propulsion of a domain wall in an antiferromagnet by magnons, *Phys. Rev. B* **90**, 104406 (2014).
- [45] O. V. Pylypovskiy, Y. A. Borysenko, J. Fassbender, D. D. Sheka, and D. Makarov, Curvature-driven homogeneous Dzyaloshinskii-Moriya interaction and emergent weak ferromagnetism in anisotropic antiferromagnetic spin chains, *Appl. Phys. Lett.* **118**, 182405 (2021).
- [46] N. M. Patrikalakis and T. Maekawa, *Shape Interrogation for Computer Aided Design and Manufacturing*, 2nd ed. (Springer, Berlin, 2002).
- [47] H. Goldstein, C. Poole, and J. Safko, *Classical Mechanics* (Addison Wesley, New York, 2000).
- [48] O. V. Pylypovskiy, D. Y. Kononenko, K. V. Yershov, U. K. Röbber, A. V. Tomilo, J. Fassbender, J. van den Brink, D. Makarov, and D. D. Sheka, Curvilinear one-dimensional antiferromagnets, *Nano Lett.* **20**, 8157 (2020).
- [49] S. Dasgupta and J. Zou, Zeeman term for the Néel vector in a two sublattice antiferromagnet, *Phys. Rev. B* **104**, 064415 (2021).
- [50] K.-W. Kim, H.-W. Lee, K.-J. Lee, and M. D. Stiles, Chirality from Interfacial Spin-Orbit Coupling Effects in Magnetic Bilayers, *Phys. Rev. Lett.* **111**, 216601 (2013).
- [51] D. Hill, V. Slastikov, and O. Tchernyshyov, Chiral magnetism: A geometric perspective, *SciPost Phys.* **10**, 078 (2021).
- [52] S. Zhang, G. Go, K.-J. Lee, and S. K. Kim,  $\text{SU}(3)$  Topology of Magnon-Phonon Hybridization in 2D Antiferromagnets, *Phys. Rev. Lett.* **124**, 147204 (2020).
- [53] W. Yu, J. Lan, R. Wu, and J. Xiao, Magnetic Snell's law and spin-wave fiber with Dzyaloshinskii-Moriya interaction, *Phys. Rev. B* **94**, 140410(R) (2016).
- [54] B. O'Neill, *Elementary Differential Geometry*, 2nd ed. (Academic Press, Boston, 2006).
- [55] S. Datta and B. Das, Electronic analog of the electro-optic modulator, *Appl. Phys. Lett.* **56**, 665 (1990).
- [56] D. H. Goldstein, *Polarized Light*, 3rd ed. (CRC Press, Boca Raton, FL, 2017).
- [57] M. V. Berry, Quantal phase factors accompanying adiabatic changes, *Proc. R. Soc. London A* **392**, 45 (1984).
- [58] V. K. Dugaev, P. Bruno, B. Canals, and C. Lacroix, Berry phase of magnons in textured ferromagnets, *Phys. Rev. B* **72**, 024456 (2005).
- [59] D. Xiao, M.-C. Chang, and Q. Niu, Berry phase effects on electronic properties, *Rev. Mod. Phys.* **82**, 1959 (2010).
- [60] R. Y. Chiao and Y.-S. Wu, Manifestations of Berry's Topological Phase for the Photon, *Phys. Rev. Lett.* **57**, 933 (1986).
- [61] R. A. Duine, K.-J. Lee, S. S. P. Parkin, and M. D. Stiles, Synthetic antiferromagnetic spintronics, *Nat. Phys.* **14**, 217 (2018).
- [62] W. Yu, Micromagnetic simulation with COMSOL MULTIPHYSICS, [www.comsol.com](http://www.comsol.com) (2021).